Nano-infrared imaging of epitaxial graphene on SiC revealing doping and thickness inhomogeneities

M. Fralaide^{1,2}, Y. Chi^{1,2}, R. B Iyer, ^{2,3}, Y. Luan^{1,2}, S. Chen², R. Shinar³, J. Shinar^{1,2,3}, M. Kolmer², M. C. Tringides^{1,2}, Z. Fei*^{1,2}

¹Department of Physics and Astronomy, Iowa State University, Ames, Iowa 50011, USA ²Ames Laboratory, U.S. Department of Energy, Iowa State University, Ames, Iowa 50011, USA ³Department of Electrical & Computer Engineering, Iowa State University, Ames, Iowa 50011, USA

ABSTRACT

We report on a nano-infrared (IR) imaging and spectroscopy study of epitaxial graphene on silicon carbide (SiC) by using scattering-type scanning near-field optical microscopy (s-SNOM). With nano-IR imaging, we reveal in real space microscopic domains with distinct IR contrasts. By analyzing the nano-IR, atomic force microscopy (AFM) and scanning tunneling microscopy (STM) imaging data, we conclude that the imaged domains correspond to single-layer graphene (SLG), bilayer graphene (BLG), and higher-doped BLG. With nano-IR spectroscopy, we find that graphene can screen the SiC phonon resonance and the screening is stronger at more conductive sample regions. Our work offers insights into the rich surface properties of epitaxial graphene and demonstrates s-SNOM as an efficient and effective tool in characterizing graphene and possibly other two-dimensional materials.

MAIN TEXT

Epitaxial graphene on silicon carbide (SiC) is a form of graphene that is grown on a SiC substrate through controlled decomposition of top SiC layers [1,2]. Compared to other scalable graphene production methods, such as chemical vapor deposition and electrochemical exfoliation of graphite, epitaxial graphene growth does not require mechanical transfer and can potentially produce graphene with high quality, low defect density, and overall better electronic properties [3]. Therefore, they are promising for electronic and optoelectronic applications (e.g., transistors, photodetectors, and quantum devices) that require graphene devices on a wafer scale. In addition, one can conveniently control the thickness of graphene with subnanometer precision by adjusting the annealing temperature and time. Moreover, the properties of epitaxial graphene can be conveniently modified during the sample growth by using chemical doping or intercalation [4-6]. With the latter method, one can tune the carrier densities, modify the band structures, and induce topological properties in graphene [7-14].

To prepare for device applications of epitaxial graphene, it is important to efficiently characterize the general sample properties such as topography, graphene thickness, and graphene doping with a high spatial resolution. The common methods used to characterize epitaxial graphene include scanning tunneling microscopy (STM), low-energy electron diffraction (LEED), Raman spectroscopy, angle-resolved photoemission spectroscopy (ARPES), and transport measurements. STM can characterize the topographical and electronic properties of the sample surface with an atomic resolution, but it is not very efficient for large-area mapping of the sample surface. LEED provides lateral and vertical information about the growth of graphene with nanoscale resolution but requires quantitative analysis [11]. The other three techniques typically lack the high spatial resolution to characterize nanoscale inhomogeneities. With Raman spectroscopy, one can determine the quality and thickness of graphene with a lateral resolution of 0.3-1 µm by monitoring the phonon resonances [15-17]. ARPES is a powerful tool for directly mapping the band structures of the sample [14]. The lateral resolution of ARPES varies from a few micrometers to hundreds of micrometer. Transport measurements can measure the electrical performance of devices across a large area of graphene. It requires complicated device fabrications and extensive modeling to decouple the substrate contribution, so it is not ideal for the fast screening of the surface properties of the epitaxial graphene.

^{*}Author to whom correspondence should be addressed: zfei@iastate.edu

The scattering-type scanning near-field optical microscopy (s-SNOM) is a type of scanning probe microscopy that can characterize the optical properties of the sample surfaces with a high spatial resolution. The principle of s-SNOM is based on the near-field interaction between the tip and the sample surface. When the tip is illuminated with a laser, strong evanescent fields (i.e., near fields) are concentrated around the tip apex that can interact strongly with the sample area right underneath the tip [see Fig. 1(a)]. As a result, the scattering signals of the tip collected by the detector contain key information about the local optical properties of the sample. As the tip is scanned across the sample, one can map out the sample's optical properties with a high spatial resolution. Our s-SNOM was built based on a tapping-mode atomic force microscope (AFM), so it can simultaneously collect optical, topographic, and mechanical information about the sample. The spatial resolution of s-SNOM is about 25 nm, which is determined by the radius of curvature at the apex of the AFM tip. The high resolution allows for detailed imaging and analysis of nanoscale structures and materials. The s-SNOM technique has been widely used in the studies of graphene produced by mechanical exfoliation [18,19] and chemical vapor deposition [20-22]. Nevertheless, s-SNOM studies of epitaxial graphene on SiC are few and are mainly focused on hydrogen-intercalated samples where the graphene layer is decoupled from the substrate due to the intercalation [23,24].

In this work, we mainly focused on pristine epitaxial graphene on SiC without intercalation, so the interactions between graphene and the substrate remain strong. Our substrates are highly N-doped 6H SiC wafers (University Wafers Inc; $\sigma = 0.02-0.2~\Omega\cdot\text{cm}$), and graphene is grown on the Si-terminated facet of the wafers. We demonstrate that the s-SNOM technique is an effective and efficient method to study the general surface properties of epitaxial graphene, which complements local high resolution STM experiments. Our samples were prepared by annealing the SiC wafer to high temperatures using the direct current heating method to select graphene thicknesses [2,14,25]. More specifically, we annealed the SiC wafer at a temperature of 1300-1350 °C, so the graphene samples as produced are predominantly bilayer graphene (BLG) with possibly a small portion of single-layer graphene (SLG) [26,27]. The excitation lasers of s-SNOM used in the work include a continuous-wave CO_2 laser and a mid-IR broadband laser, which enable both nano-IR imaging and spectroscopy. All s-SNOM experiments were performed at ambient conditions. More introductions about the s-SNOM setup are given in Supplementary Material. The STM experiments were performed *in-situ* after the UHV epitaxial graphene growth [14,28] with a variable temperature STM (Scienta Omicron) at room temperature and a low temperature STM (Scienta Omicron) at liquid nitrogen temperature (~78 K).

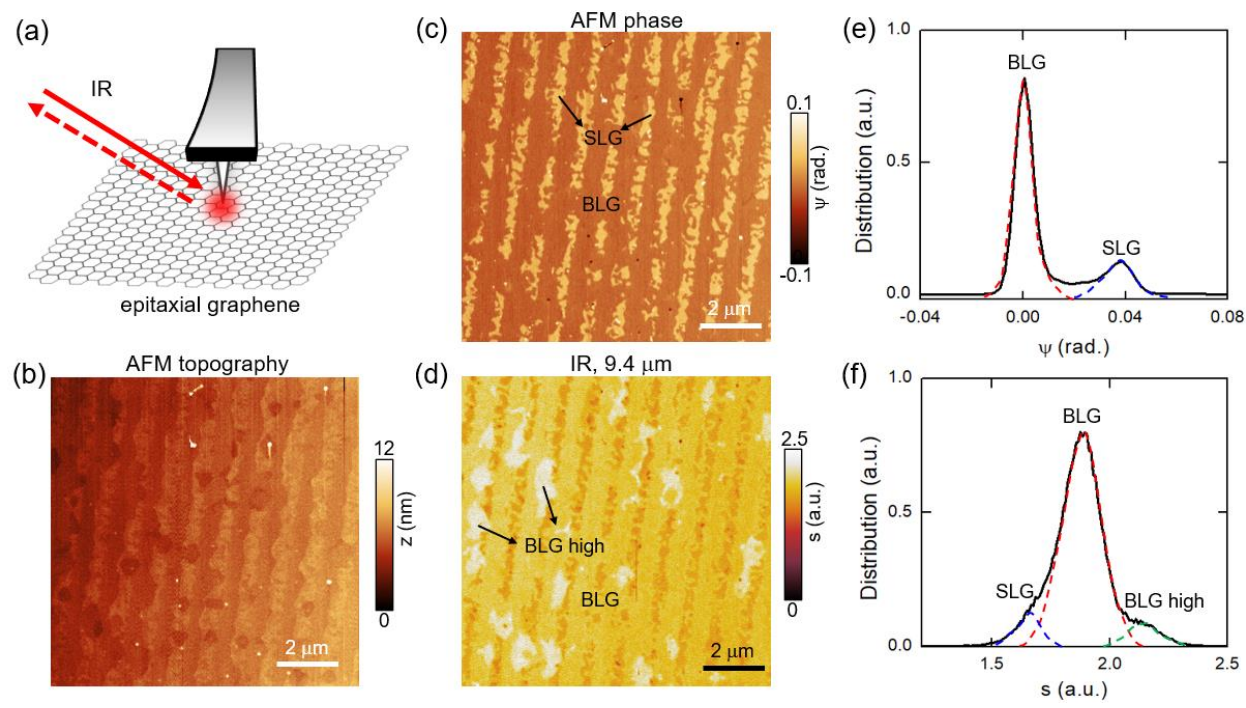


Fig. 1. (a) Illustration of s-SNOM study of epitaxial graphene on SiC. (b,c) The AFM topography and phase images of a typical sample surface of our epitaxial graphene sample. (d) The nano-IR amplitude image of the sample taken simultaneously with the AFM images in (b) and (c). The excitation laser wavelength is set to be 9.4 μ m. (e,f) Statistical distribution analysis of AFM phase and IR amplitude images in (c) and (d), respectively.

In Fig. 1(b), we present a large-area ($10 \times 10~\mu m$) AFM topography image of the sample, where one can see clear staircases on the sample surface, showing the typical terrace-step morphology – a signature feature of epitaxial graphene grown on the Si-face of SiC. The AFM phase image is shown in Fig. 1(c), where one can see two distinct phases. According to previous AFM studies of epitaxial graphene [29,30], the AFM phase is very sensitive to the thickness of graphene. This is expected because the mechanical phase of a tapping-mode AFM is a measure of the hardness of the sample surface and BLG is expected to be softer (lower AFM phase) than SLG due to the extra graphene layer that buffers further the tip from the relatively hard SiC crystal. Considering our sample growth condition (annealing temperature of 1300-1350 °C), we assign the regions with lower phase to BLG and the higher phase region to SLG. In Fig. 1(e), we show a statistical distribution analysis of the AFM phase image [Fig. 1(c)], where the two peaks are associated with SLG and BLG. The BLG peak is clearly higher than that of SLG indicating that BLG occupies more surface area of Fig. 1(c). By comparing the two distribution peaks in Fig. 1(e), we found BLG covers about ~87% of the surface area and SLG covers the rest.

Figure. 1(d) plots the IR amplitude image of the same sample area simultaneously collected with the AFM images. The excitation laser wavelength of s-SNOM here is set to be 9.4 μ m, away from the strong optical phonon of the SiC substrate at around 11 μ m (see discussions in the following paragraphs). At 9.4 μ m, SiC behaves as an insulating dielectric with only a limited contribution to the overall IR signal, so the IR contrast in Fig. 1(d) mainly reflects the optical responses of graphene. According to previous studies, IR imaging via s-SNOM is very effective in mapping conductivity inhomogeneities of a variety of samples including graphene [31-33]. This is because the near-field IR amplitude measured by s-SNOM is roughly proportional to the average reflection coefficient of all the evanescent fields [34]. The more conductive sample region tends to have a larger reflection coefficient and hence a higher IR amplitude signal. From Fig. 1(d), one can see that BLG has a slightly higher IR amplitude signal than SLG indicating that BLG has

a higher conductivity. More interestingly, we found many patches of higher-signal domains (marked as "BLG high") in the IR image in Fig. 1(d), which cannot be clearly associated with any features in AFM. An increase in IR signal at frequencies away from the SiC phonon indicates higher graphene conductivity, which can be due to either a larger thickness or higher doping. Considering that these domains are not present in the AFM phase images, we can conclude that these brighter BLG domains are due to higher doping. The origin of doping variations in our sample is not fully understood, but it is likely associated with the doping or strain inhomogeneities of the underlining SiC substrate [35-38]. More nano-IR imaging data have been collected from other regions of the sample or other samples produced under the same conditions (see Fig. S2 of Supplementary Material). In all cases, the three types of graphene domains are always present. Figure 1(f) shows the statistical distribution analysis of the IR image in Fig. 1(d). Here we found that normal BLG regions cover ~80% of the total surface area, while SLG and higher-doped BLG regions cover ~12% and ~8%, respectively. Note that we didn't observe real-space interference fringes of plasmons in our sample, which is most likely due to the strong coupling between graphene and highly-doped SiC substrate. The strong graphene-substrate coupling results in a high damping of graphene plasmons. Plasmons were observed in hydrogen-intercalated graphene samples on semi-insulating SiC substrates, where graphene appears to be quasi-freestanding [23,24].

Besides the s-SNOM experiments, we have also performed high-resolution STM imaging of the same graphene sample to verify the thickness distribution. The large-scale STM morphology shown in Fig. 2(a) depicts parallel terraces following a natural miscut of the SiC wafer along $<1\overline{1}00>$ (±0.5 degree). A zoomed-in scanning is shown in Fig. 2(b). From Fig. 2(a) and Fig. 2(b), we found two distinct types of structures within the large and elongated terraces: (I) areas surrounded by straight step edges with stepheights being multiples of a single SiC step, i.e. 0.25, 0.5, or 0.75 nm; (II) areas surrounded by meandering steps with step heights expressing a graphene thickness change (~0.3 nm), which may occur also simultaneously at a SiC step edge. In the latter case, a step height is the corresponding difference, e.g. 0.3 -0.25 = 0.05 nm or 0.75 - 0.3 = 0.45 nm [39]. Thus, the sample areas in the first case are still BLG [see blue rectangles in Fig. 2(a) and Fig. 3], while the second areas represent SLG regions [arrows in Fig. 1(c) and Fig. 2(a)]. STM topography cross-section through two discussed areas is presented in Fig. 2(c). Local high-resolution STM confirms the graphene thickness difference through graphene atomic lattice contrast difference [Fig. 2(d)] or spectroscopic signatures [40], which is however time demanding. Typical STM scanning over a relatively large sample area like that in Fig. 2(a) takes at least an hour, which is 2-3 times longer than a s-SNOM scanning. Moreover, STM requires many hours or even days of preparation to achieve ultrahigh vacuum and high stability conditions. Therefore, our s-SNOM characterization operational at ambient conditions provides convenient mesoscale determination of graphene inhomogeneities in epitaxial graphene.

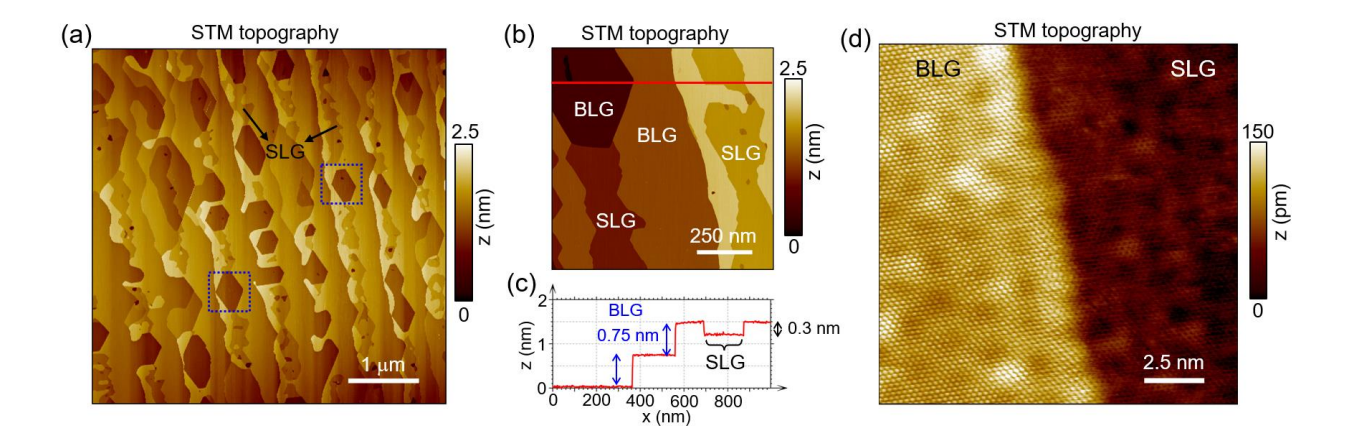


Fig. 2. (a,b) The STM topography images obtained at room temperature (+3 V; 0.5 nA). For clarity STM image in (a) was flattened by a vertical line by line processing, which resulted in the same z-scale for both panels. (c) STM cross section along the red line marked in panel (b). (d) High resolution STM image of BLG/SLG step edge obtained at liquid nitrogen temperature (+0.1 V; 0.5 nA). Note change in graphene atomic lattice contrast from 3-fold for AB-stacked BLG to honeycomb for SLG.

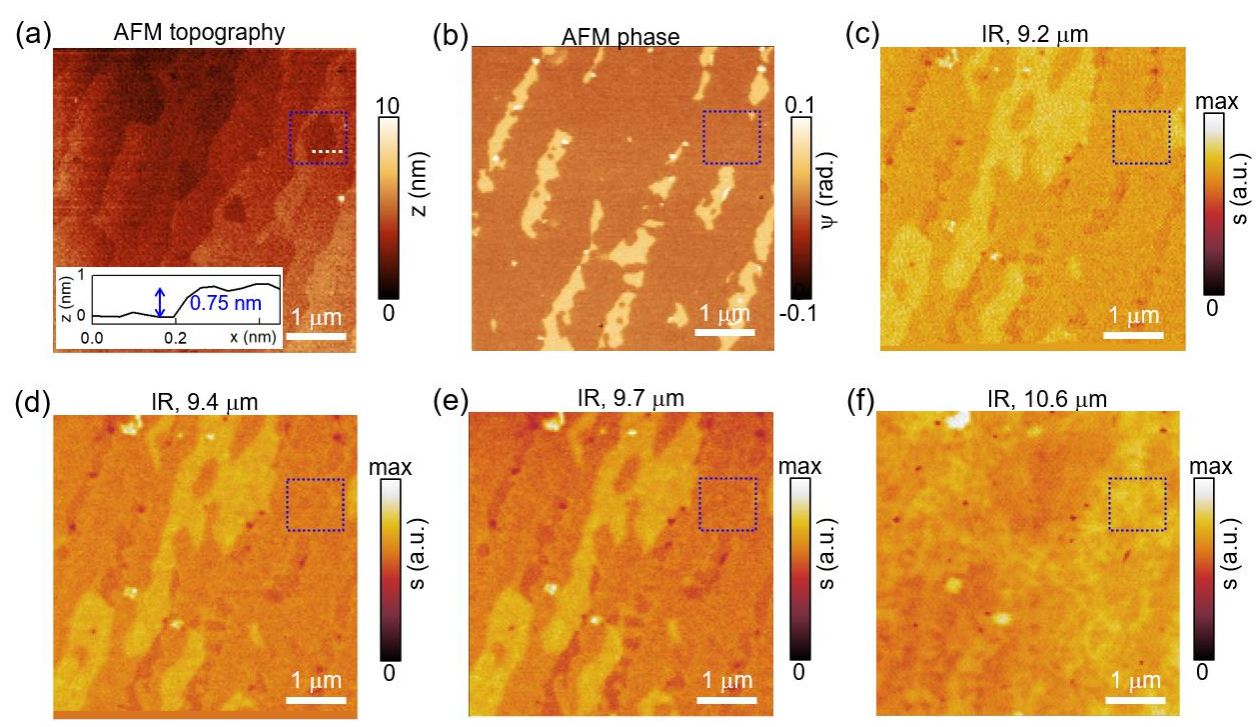


Fig. 3. (a,b) The AFM topography and phase images of a typical area of our sample. Inset plots the line profile taken along the white dashed line marked in the image. (c-f) The nano-IR amplitude images of the sample taken simultaneously with the AFM images in (a,b) at various excitation laser wavelengths. Blue, dashed squares mark a BLG region surrounded by well-defined 0.75 nm SiC step-edges (topography). Note that there is no contrast from the surrounding BLG terraces in the corresponding AFM phase and IR images.

In Fig. 3, we show additional AFM and nano-IR imaging data of our sample, where the IR images were taken at various excitation wavelengths from 9.2 to 10.6 μ m. From the IR images, one can see that SLG, normal BLG, and higher-doped BLG can be clearly distinguished from each other from 9.2 to 9.7 μ m. The IR contrasts of the three regions become stronger at 9.7 μ m than that at 9.2 μ m. As the IR wavelength increases to 10.6 μ m, no clear IR contrast can be seen among these regions. To understand such a wavelength-dependent IR contrast, we performed a nano-IR spectroscopy study of the three graphene regions. The excitation broadband laser used here covers a spectral range of 7-12 μ m. The spectra of the three graphene regions and the bare SiC wafer were shown in Fig. 4(a), where one can see a strong resonance peaked at around 11.4 μ m for all the spectra, which is originated from the optical phonon of SiC.

We first discuss the wavelength region below $10.3~\mu m$, which is off the SiC phonon resonance (see Fig. 4). Here SiC has a small IR signal, and all graphene regions have positive contrast over SiC. In addition, the signal of higher-doped BLG is stronger than that of normal BLG and SLG, which is consistent with our imaging results shown in Fig. 1 and Fig. 3. At wavelengths larger than $10.3~\mu m$, the dominant IR response is the SiC phonon resonance. Here we can see a negative contrast of graphene over SiC, i.e. graphene has a weaker signal than that of the bare SiC substrate at the resonance peak. In addition, the resonance signal of higher-doped BLG is weaker than that of normal BLG and even weaker than that of SLG. Such a negative

contrast can be understood as a screening effect of the strong phonon resonance SiC by graphene electrons. Due to the screening, the s-SNOM tip becomes less sensitive to the SiC phonons, so the phonon resonance becomes weaker. More conductive graphene regions have stronger screening effects, so higher-doped BLG has the lowest signal at around 11.3 μ m. Based on the spectroscopic data in Fig. 4(a), we found that graphene with different thicknesses and doping levels have clear contrasts from each other in the following two spectral regions: 9-10 μ m and 11-12 μ m. Therefore, these spectral regions are ideal choices for characterizing epitaxial graphene.

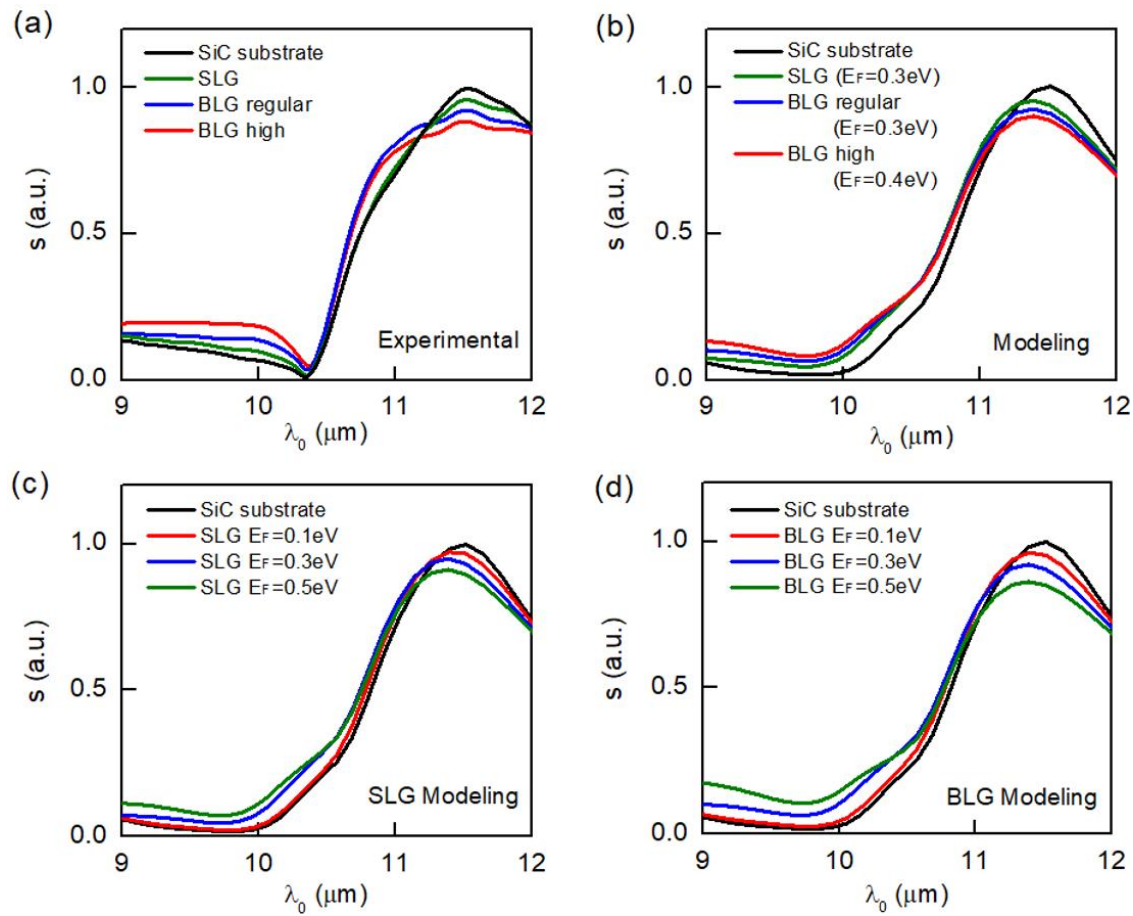


Fig. 4. (a) Experimental nano-IR spectra of SLG (green), normal BLG (blue), higher-doped BLG (red), and the bare SiC substrate (black). (b) Modeled nano-IR spectra of SLG (green), normal BLG (blue), higher-doped BLG (red), and the bare SiC substrate (black). (c,d) Modeled nano-IR spectra of SLG and BLG with various Fermi energies. The IR amplitude signals are normalized to the peak signal of the SiC substrate.

For a quantitative understanding of the IR responses of the three graphene regions, we performed numerical modeling of the nano-IR spectra using a numerical s-SNOM model based on Comsol Multiphysics. In the model, the s-SNOM tip is approximated as a conducting spheroid with a radius of curvature of 25 nm at the tip apex. Both SLG and BLG are modeled as a conducting thin layer with an optical conductivity $\sigma(\omega)$, which is sensitively dependent on the Fermi energy E_F and excitation IR frequency ω . We evaluate numerically the total radiating-dipole moment of the tip under excitations, which is roughly proportional to the nano-IR signal collected by the s-SNOM. Detailed introductions of the model and modeling parameters can be found in Supplementary Material.

The modeled spectra are plotted in Fig. 4(b), where one can see that the general features of phonon resonance are consistent with the experimental spectra in Fig. 4(a). The best match to the experimental spectra of the sample can be obtained by using $E_F = 0.3$ eV, 0.3 eV, and 0.4 eV for SLG, regular BLG, and higher-doped BLG, respectively. More modeling spectra about both SLG and BLG with various E_F settings are shown in Fig. 4(c) and Fig. 4(d) respectively. Similar to the experimental spectra, one can see clear positive and negative contrast of graphene versus the SiC substrate in the modeling spectra. These signal contrasts can be enhanced by increasing E_F . Note that E_F is approximately proportional to the Drude conductivity of graphene (see Eqs. S1 and S2 in Supplementary Material). Therefore, the near-field IR contrast of graphene observed in s-SNOM is directly linked to the free-electron responses of graphene.

In summary, we perform a systematic nano-IR imaging and spectroscopy study of epitaxial graphene on SiC using s-SNOM. With nano-IR imaging, we map the surface inhomogeneities of epitaxial graphene due to variations in thickness and doping. By modeling the s-SNOM signals, we are able to estimate the Fermi energy of both the SLG and BLG regions of the sample. Furthermore, we show with nano-IR spectroscopy that epitaxial graphene has a positive IR contrast over the substrate at spectral regions away from the phonon resonance and a negative contrast atop the resonance. The negative contrast can be understood as the screening effect of the strong SiC phonon resonance by graphene, and the screening becomes stronger at more conductive graphene regions. Our work demonstrated that s-SNOM is an effective and efficient tool for characterizing large-area epitaxial graphene samples with a high spatial resolution and hyperspectral information.

See the Supplementary Material for more information about the experimental setup, additional imaging data of epitaxial graphene, and detailed introduction about the modeling method,

Work done at Ames Lab was supported by the U.S. Department of Energy, Office of Basic Energy Science, Division of Materials Sciences and Engineering. Ames Laboratory is operated for the U.S. Department of Energy by Iowa State University under Contract No. DE-AC02-07CH11358. The nano-IR imaging and spectroscopy setup was partially supported by the National Science Foundation under Grant No. DMR1945560.

AUTHOR DECLARATIONS

Conflict of interest

The authors have no conflicts to disclose.

DATA AVAILABILITY

The data that support the findings of the study are available from the corresponding author upon reasonable request.

REFERENCES

- [1] W. Norimatsu and M. Kusunoki, Epitaxial graphene on SiC{0001}: advances and perspectives, Phys. Chem. Phys. **16**, 3501-3511 (2014).
- [2] J. Hass, W. A. de Heer, and E. H. Conrad, The growth and morphology of epitaxial multilayer graphene Journal of Physics: Condensed Matter, **20**, 323202 (2008).
- [3] G. R. Yazdi, T. Lakimov, R. Yakimova, Epitaxial Graphene on SiC: A Review of Growth and Characterization, Crystal, 6, 53 (2016).
- [4] C. Coletti, C. Riedl, D. S. Lee, B. Krauss, L. Patthey, K. von Klitzing, J. H. Smet, and U. Starke, Charge neutrality and band-gap tuning of epitaxial graphene on SiC by molecular doping, Phys. Rev. B **81**, 235401 (2010).

- [5] J. Choi, H. Lee, K.-J. Kim, B. Kim, and S. Kim, Chemical Doping of Epitaxial Graphene by Organic Free Radicals, J. Phys. Chem. Lett. 1, 505-509 (2010).
- [6] C. Chuang, Y. Yang, S. Pookpanratana, C. A. Hacker, C.-T. Liang, and R. E. Elmquist, Chemical-doping-driven crossover from graphene to "ordinary metal" in epitaxial graphene grown on SiC, Nanoscale, **9**, 11537-11544 (2017).
- [7] C. Riedl, C. Coletti, T. Iwasaki, A. A. Zakharov, and U. Starke, Quasi-Free-Standing Epitaxial Graphene on SiC Obtained by Hydrogen Intercalation, Phys. Rev. Lett. 103, 246804 (2009).
- [8] N. Briggs, Z. M. Gebeyehu, A. Vera, T. Zhao, K. Wang, A. D. L. F. Duran, B. Bersch, T. Bowen, K. L. Knappenberger Jr., and J. A. Robinson, Epitaxial graphene/silicon carbide intercalation: a minireview on graphene modulation and unique 2D materials, Nanoscale 11, 15440-15447 (2019).
- [9] S. Forti and U. Starke, Epitaxial graphene on SiC: from carrier density engineering to quasi-free standing graphene by atomic intercalation, J. Phys D: Appl. Phys. 47, 094013 (2014).
- [10] A. Yurtsever, J. Onoda, T. Iimori, K. Niki, T. Miyamachi, M. Abe, S. Mizuno, S. Tanaka, F. Komori, and Y. Sugimoto, Effects of Pb Intercalation on the Structural and Electronic Properties of Epitaxial Graphene on SiC, Small **12**, 3956-3966 (2016).
- [11] S. Chen, Y. Han, M. Kolmer, J. Hall, M. Hupalo, J. W. Evans, and M. C. Tringides, Targeted Dy intercalation under graphene/SiC for tuning its electronic band structure, Phys. Rev. B **107**, 045408 (2023).
- [12] M. Kim, M. Hupalo, M. C. Tringides, B. Schrunk, A. Kaminski, K.-M. Ho, and C.-Z. Wang, Electronic Structure of Double-Layer Epitaxial Graphene on SiC(0001) Modified by Gd Intercalation, J. Phys. Chem. C **124**, 28132-28138 (2020).
- [13] J. Wang, M. Kim, L. Chen, K.-M. Ho, M. Tringides, C.-Z. Wang, and S. Wang, Manipulation of electronic property of epitaxial graphene on SiC substrate by Pb intercalation, Phys. Rev. B **103**, 085403 (2021).
- [14] M. Kolmer, B. Schrunk, M. Hupalo, J. Hall, S. Chen, J. Zhang, C.-Z. Wang, A. Kaminski, and M. C. Tringides, Highly Asymmetric Graphene Layer Doping and Band Structure Manipulation in Rare Earth—Graphene Heterostructure by Targeted Bonding of the Intercalated Gadolinium, J. Phys. Chem. C **126**, 6863-6873 (2022).
- [15] Z. H. Ni, W. Chen, X. F. Fan, J. L. Kuo, T. Yu, A. T. S. Wee, and Z. X. Shen, Raman spectroscopy of epitaxial graphene on a SiC substrate, Phys. Rev. B 77, 115416 (2008).
- [16] J. Röhrl, M. Hundhausen, K. V. Emtsev, Th. Seyller, R. Graupner, and L. Ley, Raman spectra of epitaxial graphene on SiC(0001), Appl. Phys. Lett. **92**, 201918 (2008).
- [17] D. S. Lee, C. Riedl, B. Krauss, K. von Klitzing, U. Starke, and J. H. Smet, Raman Spectra of Epitaxial Graphene on SiC and of Epitaxial Graphene Transferred to SiO₂, Nano Lett. 8, 4320–4325 (2008).
- [18] Z. Fei, A. S. Rodin, G. O. Andreev, W. Bao, A. S. McLeod, M. Wagner, L. M. Zhang, Z. Zhao, M. Thiemens, G. Dominguez, M. M. Fogler, A. H. Castro Neto, C. N. Lau, F. Keilmann, and D. N. Basov, Gate-tuning of graphene plasmons revealed by infrared nano-imaging, Nature **487**, 82-85 (2012).
- [19] A. Woessner, M. B. Lundeberg, Y. Gao, A. Principi, P. Alonso-González, M. Carrega, K. Watanabe, T. Taniguchi, G. Vignale, M. Polini, J. Hone, R. Hillenbrand, and F. H. L. Koppens, Highly confined low-loss plasmons in graphene–boron nitride heterostructures, Nat. Mater. 14, 421-425 (2015).
- [20] Z. Fei, A. S. Rodin, W. Gannett, S. Dai, W. Regan, M. Wagner, M. K. Liu, A. S. McLeod, G. Dominguez, M. Thiemens, Antonio H. Castro Neto, F. Keilmann, A. Zettl, R. Hillenbrand, M. M. Fogler, and D. N. Basov, Electronic and plasmonic phenomena at graphene grain boundaries, Nat. Nanotechnol. **8**, 821–825 (2013).
- [21] S. G. Menabde, I.-H. Lee, S. Lee, H. Ha, J. T. Heiden, D. Yoo, T.-T. Kim, T. Low, Y. H. Lee, S.-H. Oh, and M. S. Jang, Real-space imaging of acoustic plasmons in large-area graphene grown by chemical vapor deposition, Nat. Commun. **12**, 938 (2021)
- [22] Q. Xu, T. Ma, M. Danesh, B. N. Shivananju, S. Gan, J. Song, C.-W. Qiu, H.-M. Cheng, W. Ren, and Q. Bao, Light: Science & Applications 6, 16204 (2017).
- [23] J. Chen, M. Badioli, P. A.-González, S. Thongrattanasiri, F. Huth, J. Osmond, M. Spasenović, A. Centeno, A. Pesquera, P. Godignon, A. Z. Elorza, N. Camara, F. J. G. de Abajo, R. Hillenbrand, and F. H. L. Koppens, Optical nano-imaging of gate-tunable graphene plasmons, Nature **487**, 77-81 (2012).

- [24] J. Chen, M. L. Nesterov, A. Y. Nikitin, S. Thongrattanasiri, P. Alonso-González, T. M. Slipchenko, F. Speck, M. Ostler, T. Seyller, I. Crassee, F. H. L. Koppens, L. Martin-Moreno, F. J. G. de Abajo, A. B. Kuzmenko, and R. Hillenbrand, Strong Plasmon Reflection at Nanometer-Size Gaps in Monolayer Graphene on SiC, Nano Lett. **13**, 6210-6215 (2013).
- [25] M. Hupalo, E. H. Conrad, and M. C. Tringides, Growth mechanism for epitaxial graphene on vicinal 6H-SiC(0001) surfaces: A scanning tunneling microscopy study, Phys. Rev. B **80**, 041401(R) (2009).
- [26] C. Riedl, U. Starke, J. Bernhardt, M. Franke, K. Heinz, Structural properties of the graphene-SiC(0001) interface as a key for the preparation of homogeneous large-terrace graphene surfaces, Phys. Rev. B **76**, 245406 (2007)
- [27] S. Chen, M. Horn von Hoegen, P. A. Thiel, and M. C. Tringides, Diffraction Paradox: An Unusually Broad Diffraction Background Marks High Quality Graphene, Phys. Rev. B **100**, 155307 (2019).
- [28] M. Kolmer, W. Ko, J. Hall, S. Chen, J. Zhang, H. Zhao, L. Ke, C.-Z. Wang, A.-P. Li, and M. C. Tringides, Breaking of Inversion Symmetry and Interlayer Electronic Coupling in Bilayer Graphene Heterostructure by Structural Implementation of High Electric Displacement Fields, J Phys. Chem. Lett. 13: 11571-11580 (2022).
- [29] M. Kruskopf, K. Pierz, S. Wundrack, R. Stosch, T. Dziomba, C.-C. Kalmbach, A. Müller, J. Baringhaus, C. Tegenkamp, F. J. Ahlers, and H. W. Schumacher, Epitaxial graphene on SiC: modification of structural and electron transport properties by substrate pretreatment, J. Phys.: Condens. Matter 27, 185303 (2015). [30] F. Lavini, F. Cellini, M. Rejhon, J. Kunc, C. Berger, W. de Heer, and E. Riedo, Atomic force microscopy phase imaging of epitaxial graphene films, J. Phys.: Mater. 3, 024005 (2020).
- [31] A. J. Huber, D. Kazantsev, F. Keilmann, J. Wittborn, and R. Hillenbrand, Simultaneous IR Material Recognition and Conductivity Mappingby Nanoscale Near-Field Microscopy, Adv. Mater. **19**, 2209-2212 (2007).
- [32] M. M. Qazilbash, M. Brehm, B. G. Chae, P.-C. Ho, G. O. Andreev, B. J. Kim, S. J. Yun, A. V. Balatsky, M. B. Maple, F. Keilmann, H. T. Kim, and D. N. Basov, Mott transition in VO2 revealed by infrared spectroscopy and nano-imaging, Science 318, 1750-1753 (2007).
- [33] Y. Luan, J. Qian, M. Kim, K.-M. Ho, Y. Shi, Y. Li, C.-Z. Wang, M. C. Tringides, and Z. Fei, Imaging Stacking-Dependent Surface Plasmon Polaritons in Trilayer Graphene, Phys. Rev. Applied **18**, 024052 (2022).
- [34] Z. Fei, G. O. Andreev, W. Bao, L. M. Zhang, A. S. McLeod, C. Wang, M. K, Stewart, Z. Zhao, G. Dominguez, M. Thiemens, M. M. Fogler, M. J. Tauber, A. H. Castro-Neto, C. N. Lau, F. Keilmann, and D. N. Basov, Infrared Nanoscopy of Dirac Plasmons at the Graphene-SiO₂ Interface, Nano Lett. **11**, 4701-4705 (2011).
- [35] D. A. Schmidt, T. Ohta, and T. E. Beechem, Strain and charge carrier coupling in epitaxial graphene, Phys. Rev. B **84**, 235422 (2011).
- [36] J. Eriksson, R. Pearce, T. Iakimov, C. Virojanadara, D. Gogova, M. Andersson, M. Syväjärvi, A. L. Spetz, and R. Yakimova, The influence of substrate morphology on thickness uniformity and unintentional doping of epitaxial graphene on SiC, Appl. Phys. Lett. **100**, 241607 (2012).
- [37] S. Zhang, D. Huang, L. Gu, Y. Wang, and S. Wu, Substrate dopant induced electronic inhomogeneity in epitaxial bilayer graphene, 2D Mater. 8, 035001 (2021).
- [38] D. Momeni Pakdehi, P. Schädlich, T. T. N. Nguyen, A. A. Zakharov, S. Wundrack, E. Najafidehaghani, F. Speck, K. Pierz, T. Seyller, C. Tegenkamp, and H. W. Schumacher, Silicon Carbide Stacking-Order-Induced Doping Variation in Epitaxial Graphene, Adv. Fun. Mater. **30**, 2004695 (2020).
- [39] H. Huang, W. Chen, S. Chen, and A. T. S. Wee, Huang, Bottom-up Growth of Epitaxial Graphene on 6H-SiC(0001), ACS Nano 2, 2513-2518 (2008).
- [40] P. Lauffer, K. V. Emtsev, R. Graupner, Th. Seyller, L. Ley, S. A. Reshanov, H. B. Weber, Atomic and electronic structure of few-layer graphene on SiC(0001) studied with scanning tunneling microscopy and spectroscopy, Phys. Rev. B 77, 155426 (2008).

Supplementary Material

Nano-infrared imaging of epitaxial graphene on SiC revealing doping and thickness inhomogeneities

M. Fralaide^{1,2}, Y. Chi^{1,2}, R. B Iyer, ^{2,3}, Y. Luan^{1,2}, S. Chen², R. Shinar³, J. Shinar^{1,2,3}, M. Kolmer², M. C. Tringides^{1,2}, Z. Fei^{1,2}

1. EXPERIMENTAL SETUP

To perform nano-infrared (IR) imaging and spectroscopy studies of epitaxial graphene on SiC, we used a scattering-type scanning near-field optical microscope (s-SNOM, from Neaspec GmbH). The s-SNOM is built based on an atomic force microscope (AFM), so it can simultaneously obtain both topography and optical signals of the sample. For nano-IR imaging experiments, the s-SNOM was excited by a continuous-wave CO₂ laser from Access Laser. The CO₂ laser can be tunable discretely from 9.2 to 10.8 μm. For nano-IR spectroscopy measurements, the s-SNOM was excited by a broadband pulsed laser from Toptica Photonics AG, which is constructed based on the different-frequency-generation (DFG) method. More specifically, the IR laser pulses are generated in a GaSe crystal by different-frequency mixing of near-IR pulses from an Er-doped fiber laser and synchronized supercontinuum pulses, and they have a pulse width of ~100 fs, a repetition rate of 80 MHz and an average power up to 1 mW. The spectral window of the broadband laser is set to be 8-12 μm for the measurement of the current samples. For IR detection, we used a HgCgTe (MCT) detector from Kolmar Technologies, Inc. The full optical setup is illustrated in Fig. S1, where the s-SNOM, the two lasers, and a HgCdTe detector are connected in the Michelson interferometer configuration.

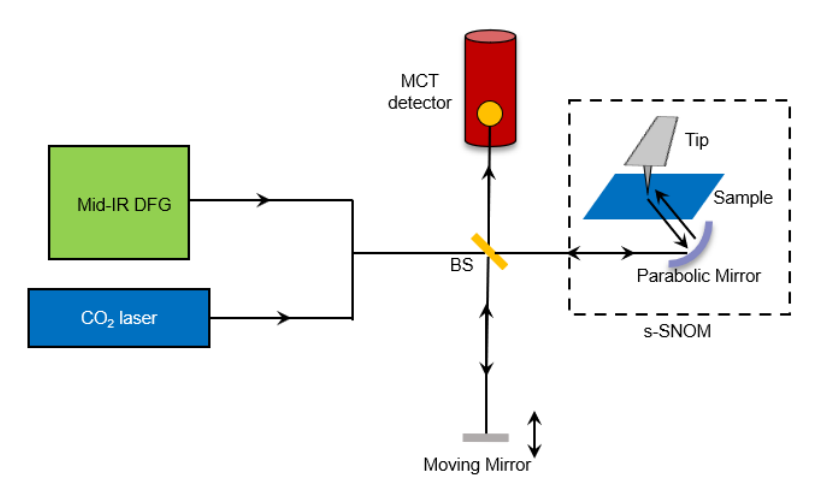


Fig. S1. Illustration of the optical setup of the s-SNOM, the two lasers, and a HgCgTe (MCT) detector connected in a Michelson interferometer configuration.

2. ADDITIONAL IMAGING DATA

In Fig. S2, we present additional imaging data of two epitaxial graphene samples. The first sample shown in Fig. S2(a-c) is the same as that studied in Figs. 1-4, but at different regions of the sample. The

¹Department of Physics and Astronomy, Iowa State University, Ames, Iowa 50011, USA

²Ames Laboratory, U.S. Department of Energy, Iowa State University, Ames, Iowa 50011, USA

³Department of Electrical & Computer Engineering, Iowa State University, Ames, Iowa 50011, USA

images shown in Fig. S2(d-f) were from a different sample produced under the same growth conditions. For both samples, we plot the AFM topography, AFM phase, and nano-IR images. The IR images were taken at the excitation wavelength of 9.4 µm. The general features observed in Fig. S2 are consistent with those in Figs. 1-4. In all cases, we observed typical staircase structures in AFM topography images, mixed SLG and BLG regions in the AFM phase images, and distinct IR contrasts from different sample regions (i.e., SLG, regular BLG, and higher-doped BLG) in the nano-IR images.

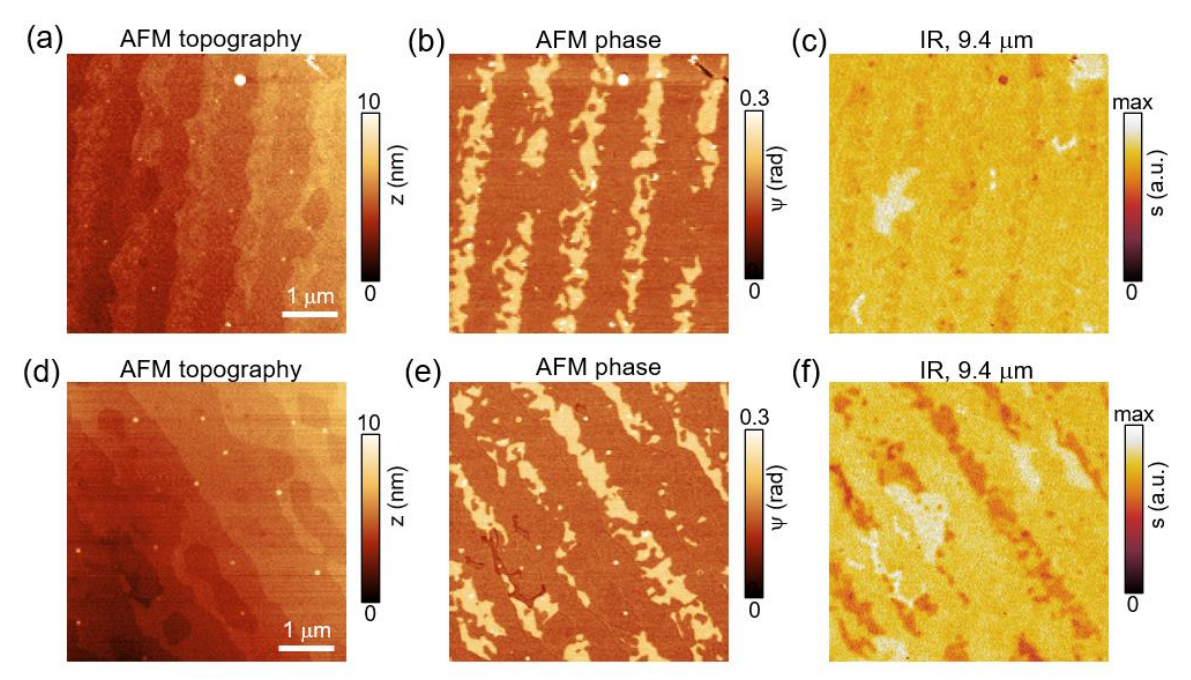


Fig. S2. Additional AFM topography, AFM phase, and nano-IR imaging data of sample 1 (a-c) and sample 2 (d-f).

3. MODELING OF THE NANO-IR SPECTRA

To calculate the nano-IR spectra, we construct a numerical model based on Comsol Multiphysics. The model is set to be axisymmetric along the axis of the tip (z axis), which has a much higher computation efficiency than a pure 3D model. In the model, the s-SNOM tip was approximated as a spheroid with a radius of curvature of 25 nm at the tip apex. The length of the tip is set to be 100 times the tip radius. The signal collected by the s-SNOM detector is proportional to the z-axis polarization (p_z) of the tip. As discussed in the main text, the scattering-type scanning near-field optical microscope (s-SNOM) is typically based on a tapping-mode atomic force microscope (AFM). Due to the tip-tapping, the s-SNOM signal is modulated. Demodulating the s-SNOM signal at higher harmonics of the tapping frequency could generate genuine near-field signals. Our quantitative model computes accurately the s-SNOM signals by considering the tip modulation & demodulation acquisition process. More introductions to the model and signal acquisition process can be found in Ref. S1.

In the model, the sample was constructed as a two-layer system with graphene (SLG or BLG) as the top layer and a thick SiC layer as the bottom layer (thickness = 1 μ m). For the SiC layer, we adopted the analytical dielectric function $\varepsilon(\omega)$ from Ref. S2, which is written as a sum of a single-phonon oscillator and a Drude relaxation term. The modeling parameter of graphene is the optical conductivity $\sigma(\omega, E_F)$, where ω is the IR frequency and E_F is the Fermi energy. The optical conductivity has components due to both intraband transitions and interband transitions. The interband components have a very small impact on the responses of our graphene sample due to the relatively high doped level ($E_F > 0.2$ eV) and relatively low IR energy of our laser (E < 0.2 eV). Interband transitions are enabled at high frequencies when E is

closer or higher than $2E_F$ or the interlayer hopping energy of bilayer graphene $\gamma \approx 0.39$ eV. We show below the analytical formula of both SLG and BLG of the intraband component (i.e., Drude conductivity) following Ref. S3.

$$\sigma_{SLG}(\omega, E_F) = \frac{e^2 E_F}{\pi \hbar^2} \frac{i}{\omega + i\Gamma}$$
 [S1]

$$\sigma_{BLG}(\omega, E_F) = \frac{2e^2 E_F}{\pi \hbar^2} \left[\frac{(E_F + \gamma)}{2E_F + \gamma} + \frac{(E_F - \gamma)}{2E_F - \gamma} \Theta(E_F - \gamma) \right] \frac{i}{\omega + i\Gamma}$$
 [S2]

References for Supplementary Material:

- [S1] Y. Luan, L. McDermott, F. Hu, and Z. Fei, Tip-and plasmon-enhanced infrared nanoscopy for ultrasensitive molecular characterizations, Phys. Rev. Applied **13**, 034020 (2020).
- [S2] S. Amarie and F. Keilmann, Broadband-infrared assessment of phonon resonance in scattering-type near-field microscopy, Phy. Rev. B **83**, 045404 (2011)
- [S3] E. J. Nicol and J. P. Carbotte, Optical conductivity of bilayer graphene with and without an asymmetry gap, Phys. Rev. B 77, 155409 (2008).